High-power performance and analysis of six X-band high-gradient accelerating structures

Heng Deng, Hao Zha, Jiaru Shi,* Qiang Gao, Yingchao Du, Boyuan Feng, Xiancai Lin, Hongyu Li, Jian Gao, Fangjun Hu, Qingzhu Li, Weihang Gu, Wenhui Huang, Chuanxiang Tang, and Huaibi Chen

Department of Engineering Physics, Tsinghua University, Beijing 100084, China
and Key Laboratory of Particle and Radiation Imaging, Tsinghua University, Ministry of Education, Beijing 100084, China

(Received 4 June 2025; accepted 29 April 2026; published 29 May 2026)

Six X-band accelerating structures with identical radio frequency (rf) designs have been developed and fabricated for the Very Compact Inverse Compton Scattering Gamma-Ray Source (VIGAS) project at Tsinghua University, representing the first large-scale deployment of such devices with consistent rf performance in China. This article presents the tuning, conditioning, and high-power performance results of these structures, with emphasis on in-depth analysis of conditioning processes and rf breakdown phenomena. The six structures achieved an accelerating gradient of 80 MV/m with a breakdown rate of no more than 1×10^{-4} per pulse after systematic conditioning. Our study reveals several critical aspects of rf breakdown behavior in X-band high-gradient accelerating structures. Key observations include the localization of breakdown events in regions of high electric field, particularly in cells adjacent to the input coupler; a power-law dependence of the normalized breakdown rate on cumulative pulse count, with notable variation in fitting parameters across different structures; and a two-exponential statistical distribution characterizing breakdown intervals. These findings offer important implications for optimizing conditioning strategies for high-gradient rf structures. Furthermore, the analysis of performance variations among nominally identical structures uncovers underlying physical mechanisms governing breakdown, establishing a useful benchmark for the development of future compact accelerator facilities.

DOI: 10.1103/23fy-29ff

I. INTRODUCTION

The Very Compact Inverse Compton Scattering Gamma-Ray Source (VIGAS), currently under development at Tsinghua University, is a next-generation γ-ray light source designed to produce high-flux, tunable gamma rays. The system targets a rate of 10^8 photons per second with an adjustable energy range of 0.2–4.8 MeV, achieved via collisions between a relativistic electron beam (tunable between 50 and 350 MeV) and an 800 or 400 nm laser. The electron beam is optimized for high brightness, with a normalized emittance below 0.6 μm [1–6]. The complete system, as shown in Fig. 1, occupies less than 15 m and enables applications including nuclear resonance fluorescence spectroscopy, ultrahigh resolution γ-ray imaging, and radioisotope production studies [7–9]. This demanding requirement makes X-band high-gradient (HG) accelerating technology, which enables significantly higher accelerating gradients than conventional S-band or C-band structures, a pivotal choice.

The pursuit of high gradients in X-band accelerating structures has been driven by international efforts in linear collider research, such as the Global Linear Collider, Next Linear Collider, and Compact Linear Collider programs [10–16]. These initiatives have demonstrated that operational gradients exceeding 100 MV/m are feasible [17–19], establishing X-band as a key technology for future compact accelerators. However, a primary limitation at these high gradients is radio frequency (rf) breakdown. The process of conditioning, systematically exposing a structure to increasing rf power to mitigate breakdowns, is essential for achieving operational stability. While the conditioning phenomenon is well known, the statistical evolution of the breakdown rate (BDR) and its dependence on structure-specific factors remain areas of active investigation, particularly for ensembles of identical structures.

This article presents the first large-scale deployment and systematic analysis of identical X-band HG accelerating structures in China. The six structures named XT72 were fabricated using uniform processes, sharing an identical

*Contact author: shij@tsinghua.edu.cn

Published by the American Physical Society under the terms of the Creative Commons Attribution 4.0 International license. Further distribution of this work must maintain attribution to the author(s) and the published article's title, journal citation, and DOI.

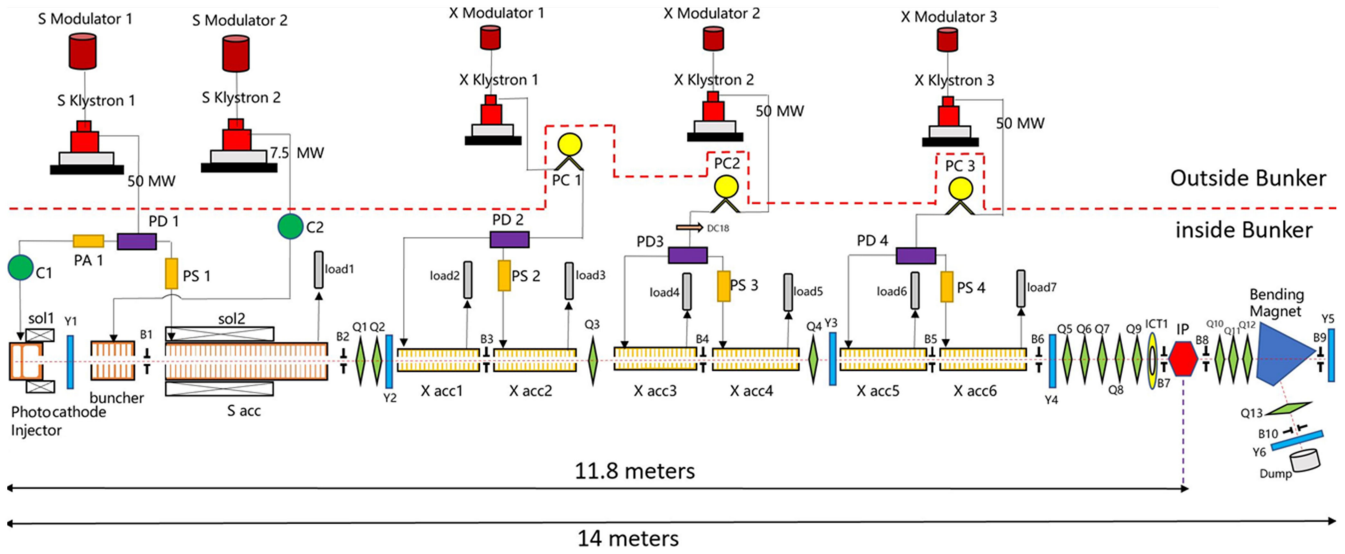


FIG. 1. Layout of the accelerator system of VIGAS facility. Abbreviations in this figure are defined as follows: PC, pulse compressor; PD, power divider; PA/PS, power attenuator/phase shifter; C, circulators; acc, accelerator; sol, solenoid; Y, YAG screen; B, beam position monitor; Q, quadrupole; ICT, integrated current transformer; IP, interaction point; FC, Faraday cup.

design, consisting of 70 regular cells and 2 coupler cells per structure, with a target gradient of 80 MV/m and a specified BDR below 1×10^{-4} per pulse [3,4]. Following successful low-power rf tuning confirmed by reflection coefficients under -25 dB and phase advances of $120 \pm 0.1°$, the structures underwent high-power conditioning and performance evaluation. Our work emphasizes the comparative analysis of a multistructure dataset to extract general insights into high-power behavior of X-band HG structures. Key aspects of this investigation include mapping the spatial distribution of rf breakdowns, revealing localized hotspots near high-field regions such as the input coupler, and analyzing the evolution of the breakdown rate throughout conditioning. We show that the modified BDR follows a power-law dependence on the cumulative number of rf pulses, similar to previous studies [20], and by aggregating data across all six structures, we establish quantitative parameters that describe this evolution. These findings provide statistical characterization of breakdown location and rate dynamics, delivering benchmark data and methodologies essential for improving the reliability and predictability of X-band high-gradient technology in future accelerator applications.

This article is organized as follows. We begin with an overview of the rf design of the structures, detailing key parameters. We then describe the low-power rf measurements and tuning procedures, discussing the consistency of the results across the structures. Finally, we focus on the high-power conditioning process, analyzing the breakdown rate evolution, spatial distribution of rf breakdown events, and the maximum achieved gradients. It is anticipated that this work will provide valuable insights for future research into rf breakdown phenomena.

II. X-BAND ACCELERATING MODULE

The VIGAS X-band linac is organized into three identical modules as shown in Fig. 1, each containing two X-band accelerating structures [21]. Each module is powered by a pulse modulator that drives an X-band klystron, delivering 50 MW of peak rf power with pulse durations up to 2 μs at a repetition rate of 10 Hz. rf power is delivered via a circular waveguide to a SLED-like pulse compressor, achieving a power gain of 4.5. The rf power is subsequently evenly distributed to the 3 dB hybrid couplers, each of which drives an X-band accelerating structure, achieving a total accelerating voltage of 100 MV across the rf module.

The accelerating structure operated at 11.424 GHz with a phase advance of $2\pi/3$. To reduce the quadrupole field component of the coupler, the coupler adopts a racetrack shape design. To maintain a uniform longitudinal electric field distribution, the structure incorporates progressively tapered iris apertures along its length. This tapering profile compensates for rf power attenuation, enabling a constant accelerating gradient to be sustained when driven by a flattop rf pulse. A comprehensive list of parameters for the accelerating structure's design is given in Table I. The normalized breakdown rate BDR* evaluates acceleration structures at varying pulse width [20]:

$$\mathrm{BDR}^* = \frac{\mathrm{BDR}}{E^{30}\tau^5}, \tag{1}$$

where E is accelerating gradient and τ is pulse width. The modified Poynting vector is defined as [22,23]:

$$S_c = |\mathrm{Re}(S)| + g_c|\mathrm{Im}(S)| \tag{2}$$

TABLE I. Primary rf parameters of XT72.

Properties	Value
Frequency (GHz)	11.424
Mode	$2\pi/3$
Aperture radius (mm)	3.92 – 3.12
v_g/c	0.0322 – 0.0146
Accelerating gradient (MV/m)	80
Filling time (ns)	98
Shunt impedance (MΩ/m)	93 – 109
$E_{s,\max}$@80 MW(MV/m)	185
$S_{c,\max}$@80 MW(MW/mm^2)	4.62
$H_{\parallel}$@80 MW(kA/m)	456

with S being the rf field's Poynting vector. Surface magnetic fields induce pulsed heating, critical in couplers. For copper structures working at X-band, heating estimation follows [24,25]:

$$\Delta T = 137||H_{\parallel}||^2\sqrt{f_0 t_p}, \tag{3}$$

where ΔT (℃) depends on $H_{\parallel}$ (MA/m), frequency f (GHz), and pulse length t_p (μs).

III. TUNE AND LOW-POWER TEST

Functionality of the HG structures was verified via tuning and low-power rf tests using the nonresonant bead-pull method [26] for field distribution measurement and a tuning method based on local reflection [27,28] to improve tuning efficiency and accuracy. The six XT72 structures (labeled No. 1–No. 6) all underwent meticulous low-power rf characterization, including S-parameter and bead-pull measurements, to validate their electromagnetic performance for integration into the VIGAS system. S-parameter measurements, conducted using a vector network analyzer (VNA), provided crucial data on the reflection (S_{11}) and transmission (S_{21}) coefficients, facilitating a thorough assessment of rf behavior, as illustrated in Fig. 2. Minimizing reflection coefficients is paramount, as high reflection can lead to wasted microwave power and potential damage to the power source; our measurements confirm that the reflection coefficient for each structure at the operating frequency is maintained below −25 dB. Figure 3 illustrates the axial electric field distributions achieved post-tuning, while Fig. 4 presents a comparative analysis of the phase advance measurements obtained before and after tuning for all six structures. The apparent length differences among structures in Fig. 3 arise from the manual trigger mode of the VNA used for bead-pull measurements: Random selections of trigger time and sampling points for each structure resulted in distinct unit length scalings in the plots. All structures are fabricated to identical physical lengths with no actual dimensional differences. Furthermore, given that the ideal amplitude distribution of the electric field for a constant-gradient structure approximates a flattop, we employ the standing wave ratio (SWR), derived from transmission line theory, to quantify the flatness of the electric field. SWR is defined as

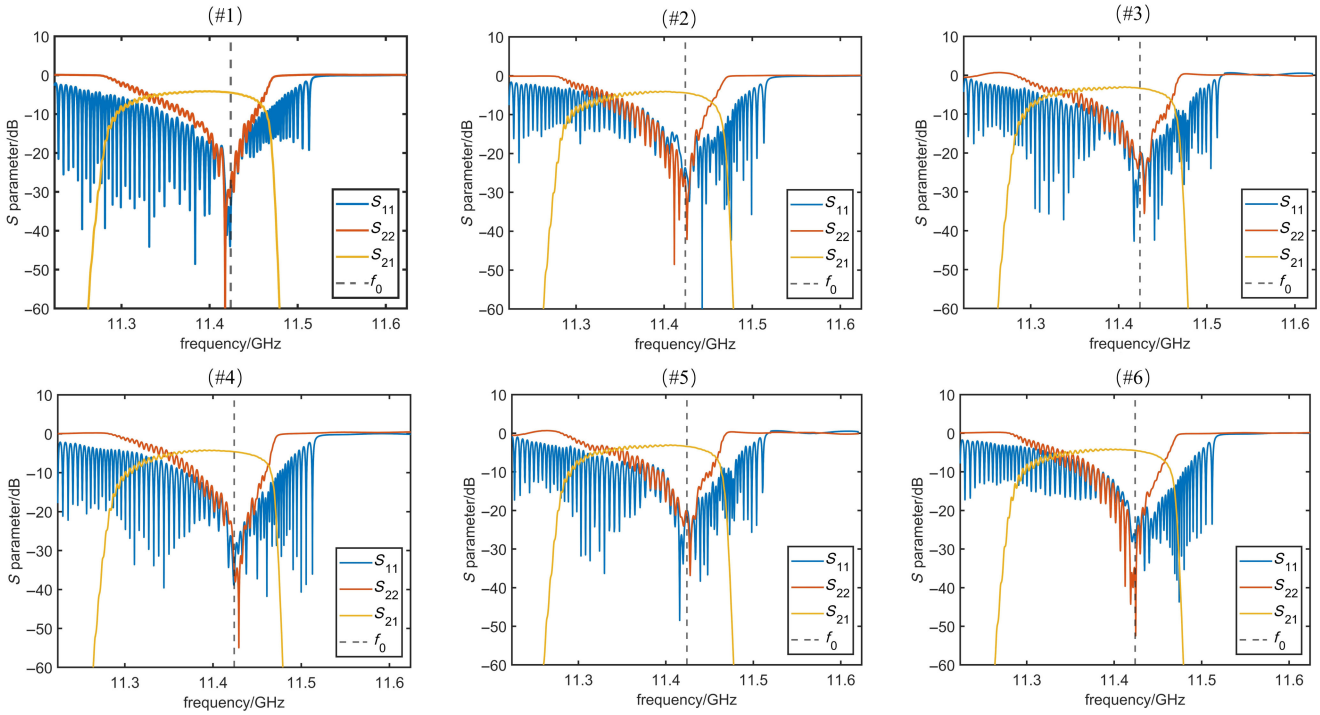


FIG. 2. S-parameter after tuning of XT72 No. 1–No. 6.

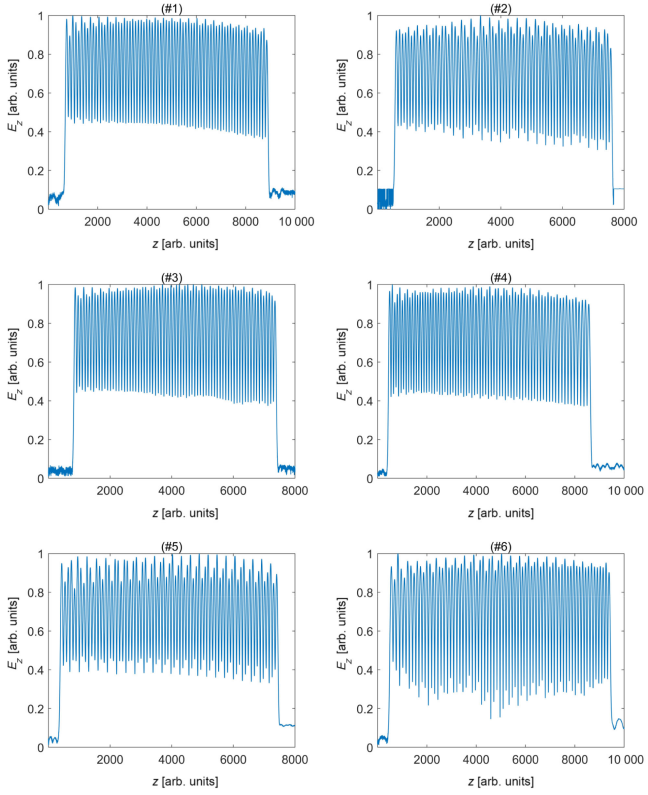


FIG. 3. Field distribution of XT72 after tuning.

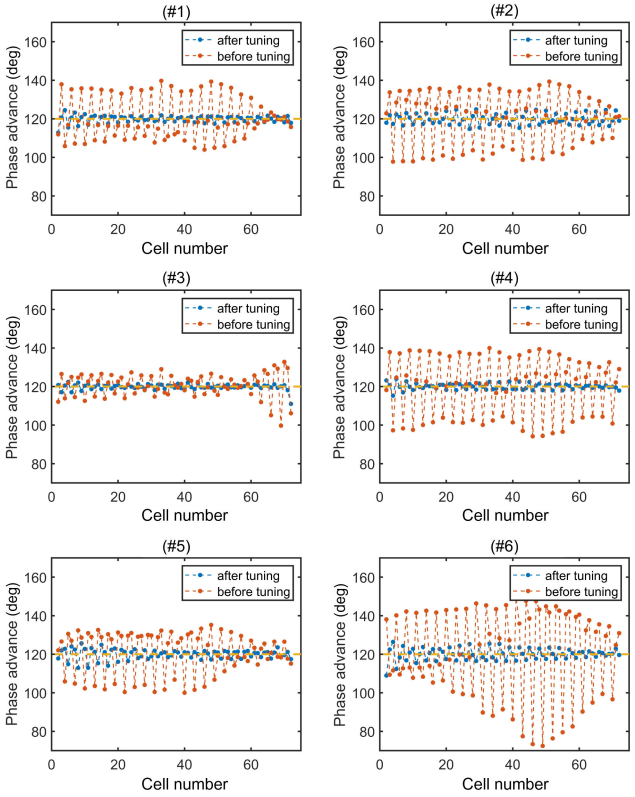


FIG. 4. Phase advance of XT72 before and after tuning.

$$\mathrm{SWR} = \frac{\max(E_{\mathrm{peak}})}{\min(E_{\mathrm{peak}})}, \tag{4}$$

where E_{peak} represents the peak value of the axial electric field, and max/min denote the maximum and minimum values, respectively. In summary, the S-parameters at the operating frequency, the average phase advance after tuning (ϕ_0) and its standard deviation (σ_{ϕ_0}), the average phase advance before tuning (ϕ_0') and its standard deviation ($\sigma_{\phi_0'}$), and the SWR after tuning are presented in Table II. These test results collectively demonstrate the successful optimization of all six X-band HG accelerating structures for seamless integration into the VIGAS system.

IV. HIGH-POWER TEST

High-power conditioning of the XT72 structures was conducted at the Tsinghua University TPOT-X facility [29]. A two-phase strategy was implemented: first, short-pulse (80 ns) conditioning was used to rapidly achieve a gradient of 80 MV/m; second, pulse-width optimization was performed by reducing the gradient to 80% of its design value while extending the pulse width to 120 ns. Power increments were applied until a reflected signal exceeded a predefined threshold (triggering an immediate low-level rf (LLRF) interlock), which was defined as breakdown detection. As illustrated in Figs. 5 and 6, the six XT72 structures required an average of approximately 12 million pulses to reach 80 MV/m at a 120 ns pulse width, corresponding to a BDR of approximately 1×10^{-4}/pulse.

TABLE II. Summary of tuning results for XT72.

Structure	XT72 No. 1	XT72 No. 2	XT72 No. 3	XT72 No. 4	XT72 No. 5	XT72 No. 6
S_{11} (dB)	−28.05	−31.92	−37.32	−35.45	−28.11	−25.24
S_{21} (dB)	−4.45	−4.39	−4.61	−4.54	−3.43	−4.51
ϕ_0 (deg)	119.97	120.12	119.91	119.99	120.02	120.11
σ_{ϕ_0} (deg)	1.85	2.87	1.84	1.58	2.61	3.16
ϕ_0' (deg)	120.12	120.19	120.67	120.05	120.82	121.17
$\sigma_{\phi_0'}$ (deg)	10.87	13.78	6.12	15.15	10.97	22.61
SWR	1.14	1.19	1.09	1.11	1.24	1.21

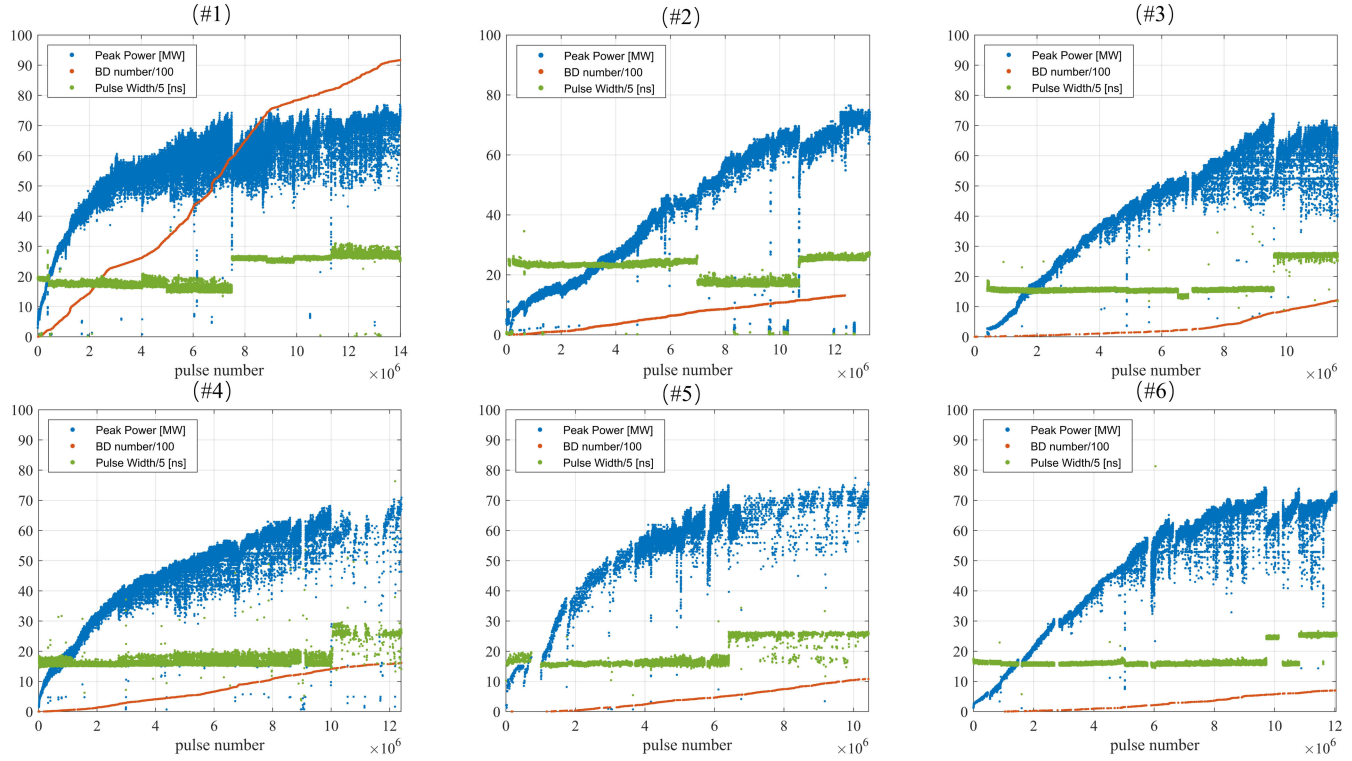


FIG. 5. Conditioning history of XT72 No. 1–No. 6, blue line is input power, green line is pulse width, and red line is accumulated rf breakdown.

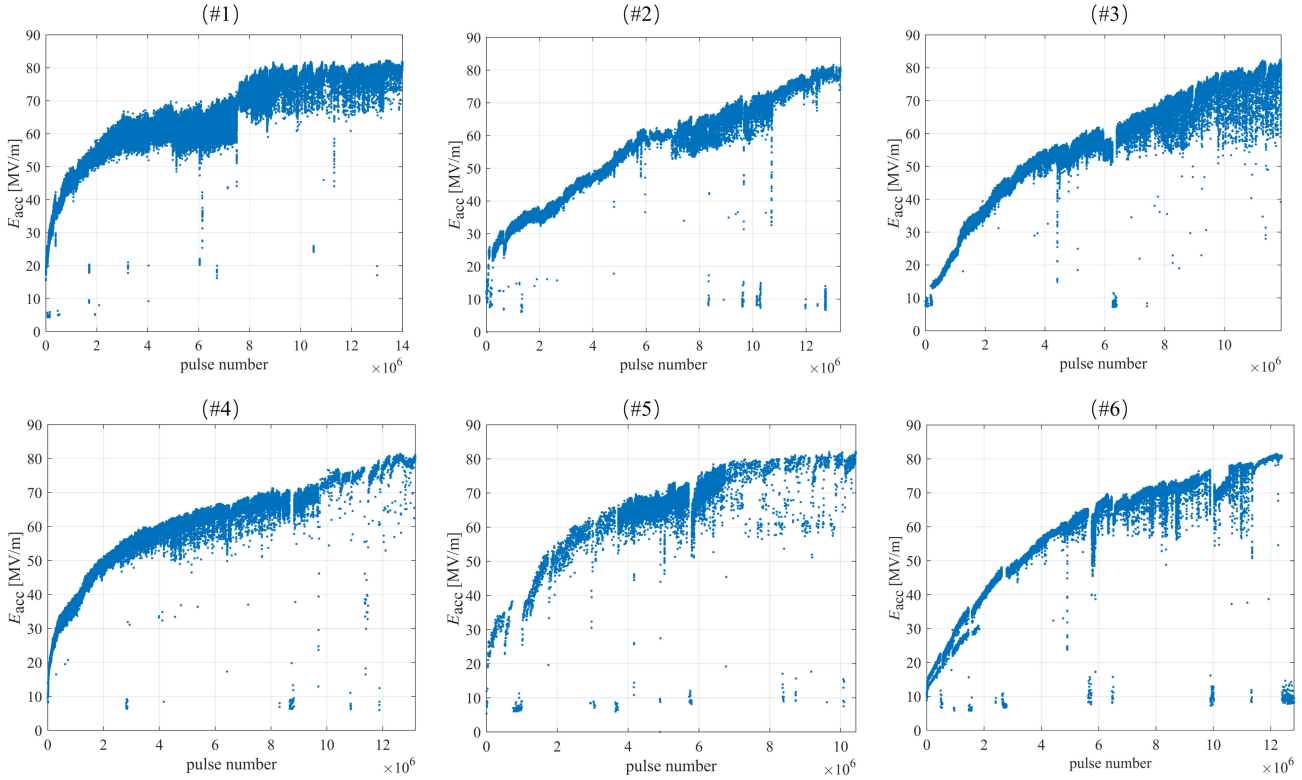


FIG. 6. Conditioning history of XT72 No. 1–No. 6 for accelerating gradient.

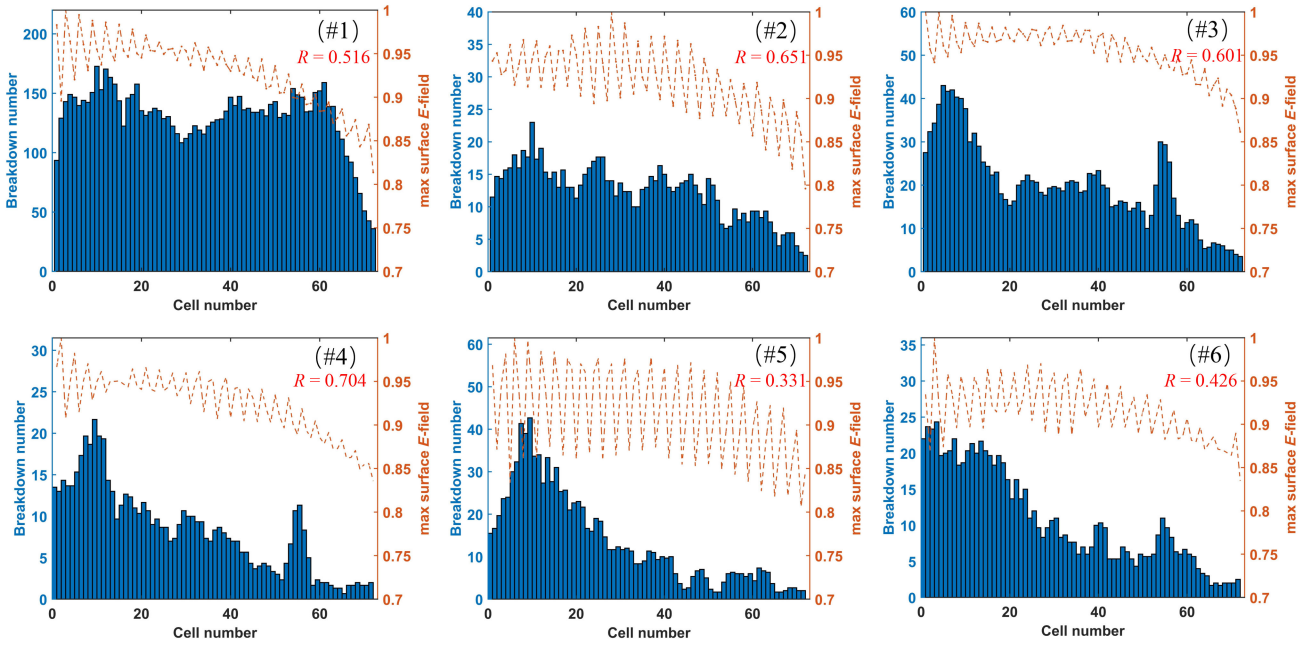


FIG. 7. Accumulated rf breakdown and maximum surface electric field in each cell of XT72 No. 1–No. 6.

The accelerating gradient in Fig. 6 was calculated using the following equation:

$$E_{\mathrm{acc}}(t) = \frac{1}{L}\int_0^L \sqrt{\frac{\omega r(z) P[t-\tau(z)]}{v_g(z)Q(z)}} e^{-\alpha(z)} H[t-\tau(z)]\mathrm{d}z, \tag{5}$$

where $P(t)$ is the incident power of the structure, α denotes the power attenuation factor along the structure, τ represents the signal time delay, and H is the Heaviside function. However, XT72 No. 1 showed an exceptionally high cumulative number of breakdowns, mainly due to the adoption of a more aggressive conditioning strategy and shorter power step time, which were improved in the conditioning of subsequent structures.

The longitudinal distribution of rf breakdowns was analyzed using the input, transmitted, and reflected rf signals. When a breakdown occurs within the structure, it acts as a localized short circuit and instantaneously reflects all subsequent rf power. The transmitted pulse is therefore truncated, with its duration (t_{tr}) directly indicating the time of the breakdown within the input pulse. The reflected pulse, captured by a directional coupler, exhibits a time delay (t_{re}) relative to the input pulse. This delay corresponds to the round-trip time for the rf wave to travel from the input coupler to the breakdown location and back. Therefore, the breakdown location was defined by the following relation [30–32]:

$$2\sum_{i=1}^{n}\frac{L_{\mathrm{cell}}}{v_{g_i}} > t_{re} - t_{tr} \geq 2\sum_{i=1}^{n-1}\frac{L_{\mathrm{cell}}}{v_{g_i}}, \tag{6}$$

where L_{cell} is the length of a single cell, v_{g_i} is the group velocity of the ith cell, and n is the cell index number where breakdown happens. An instance of rf waveforms of both transmitted and reflected power for normal and breakdown pulses is provided in Fig. 8. It should be emphasized that this localization technique relies on the relative timing between the rising edge of the reflected pulse and the falling edge of the transmitted pulse. The spatial resolution is limited by signal dispersion and the accuracy of edge detection; accordingly, the breakdown distributions shown in Fig. 7 have been smoothed to account for this uncertainty.

To quantitatively relate the observed breakdown distribution to the electromagnetic design, we analyzed the correlation between the cumulative number of breakdowns in each cell and the corresponding maximum surface electric field, normalized to 1. The surface field values were derived from the tuning results and rf design. As shown in Fig. 7, a clear spatial correlation is evident, with cells near the input coupler exhibiting significantly higher

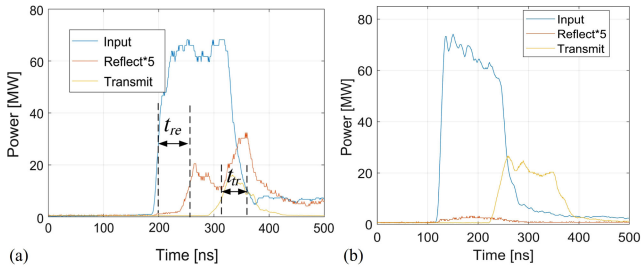


FIG. 8. Power waveform instances of XT72, (a) breakdown waveform and (b) normal waveform.

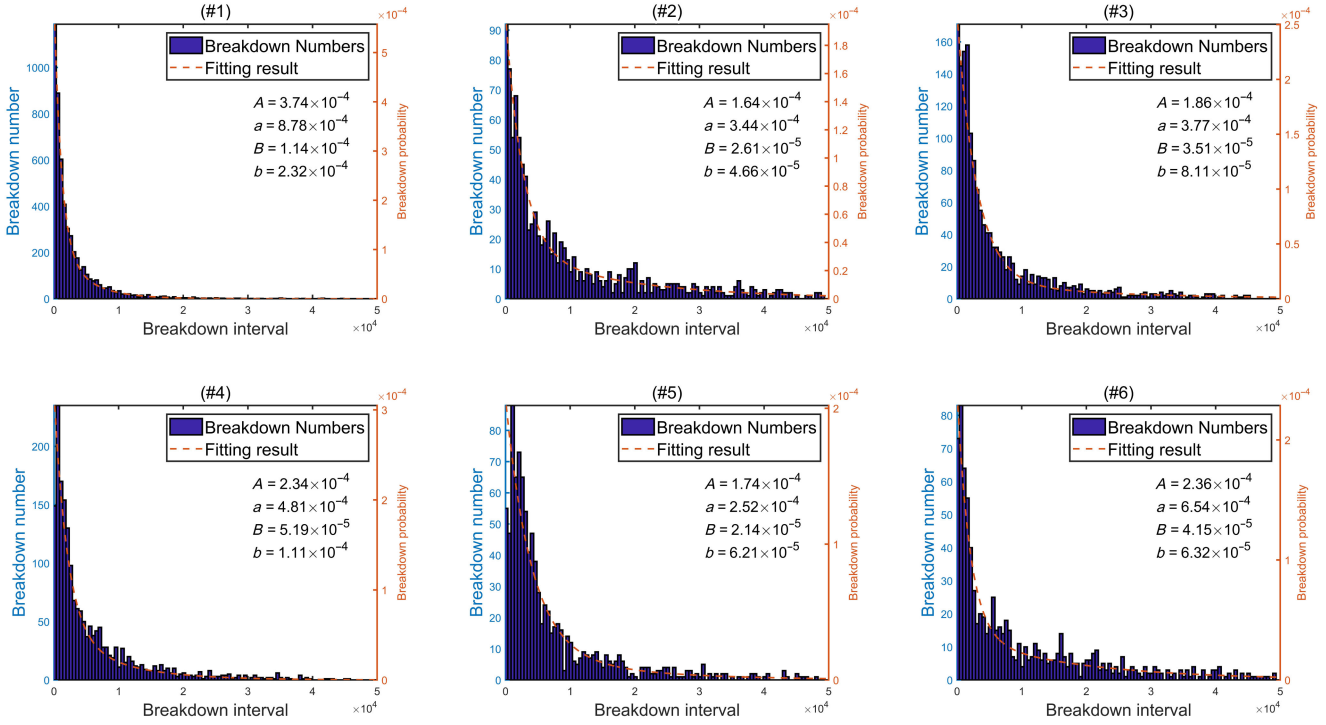


FIG. 9. rf breakdown interval distribution and fit results of XT72 No. 1–No. 6.

breakdown rates. This correlation was quantified using the Pearson correlation coefficient, which yielded a value of $R = 0.538$, providing statistical evidence that regions with enhanced surface fields experience higher breakdown probability. This finding is consistent with observations in similar high-gradient structures, such as the C-band modules of SwissFEL [33], and physically explains the concentration of breakdown events near the input coupler. Notably, the relatively lower correlation coefficients observed in XT72 No. 5 and XT72 No. 6 are attributed to an abnormally large standing-wave component of rf field in these structures.

It has been reported and verified by experiments that the probabilistic behavior of breakdowns may be described by the sum of two exponential terms [30,34,35]:

$$pdf(n_p) = Ae^{-an_p} + Be^{-bn_p}, \tag{7}$$

where *pdf* is the probability density function of the number of pulses between subsequent breakdowns, and n_p denotes the rf pulse numbers between two adjacent breakdowns. Of the two exponential items, one represents the long-term distribution of breakdowns, and these events are called primary events. The other is considered to represent the increase in breakdown caused by primary events, and the corresponding events are called secondary events. Figure 9 shows breakdown distribution of XT72 No. 1–No. 6 and the corresponding fitting curves. The value of all fitting parameters are shown in Table III. A comparative analysis of the fitting parameters in Table III reveals notable variations among the six structures, particularly in the secondary breakdown rate (b). For instance, structure XT72 No. 1 exhibits the highest value of B and a relatively large b, consistent with its aggressive conditioning history which likely generated more particulates, leading to a higher rate of secondary events. In contrast, structures conditioned with more conservative protocols (e.g., XT72 No. 3 and No. 5) show lower values of b, indicating a more stable state with fewer secondary-triggered breakdowns. In order to clarify the statistical nature of the breakdown distribution, we divided the breakdown data into three subsets and present their distributions separately. These three subsets are the first 200 breakdowns, breakdowns from the first conditioning phase, and breakdowns from the second conditioning phase. During the first 200 breakdowns, the BDR was relatively low, and the breakdown distribution deviated slightly from the double-exponential distribution, likely due to statistical fluctuations. In the second conditioning phase, the pulse

TABLE III. Fitting parameters of XT72.

Structure	A	a	B	b
XT72 No. 1	3.75×10^{-4}	8.78×10^{-4}	1.14×10^{-4}	2.32×10^{-4}
XT72 No. 2	1.64×10^{-4}	3.44×10^{-4}	2.61×10^{-5}	4.66×10^{-5}
XT72 No. 3	1.86×10^{-4}	3.77×10^{-4}	3.51×10^{-5}	8.11×10^{-5}
XT72 No. 4	2.34×10^{-4}	4.81×10^{-4}	5.19×10^{-5}	1.11×10^{-4}
XT72 No. 5	1.74×10^{-4}	2.52×10^{-4}	2.14×10^{-5}	6.21×10^{-5}
XT72 No. 6	2.36×10^{-4}	6.54×10^{-4}	4.15×10^{-5}	6.32×10^{-5}

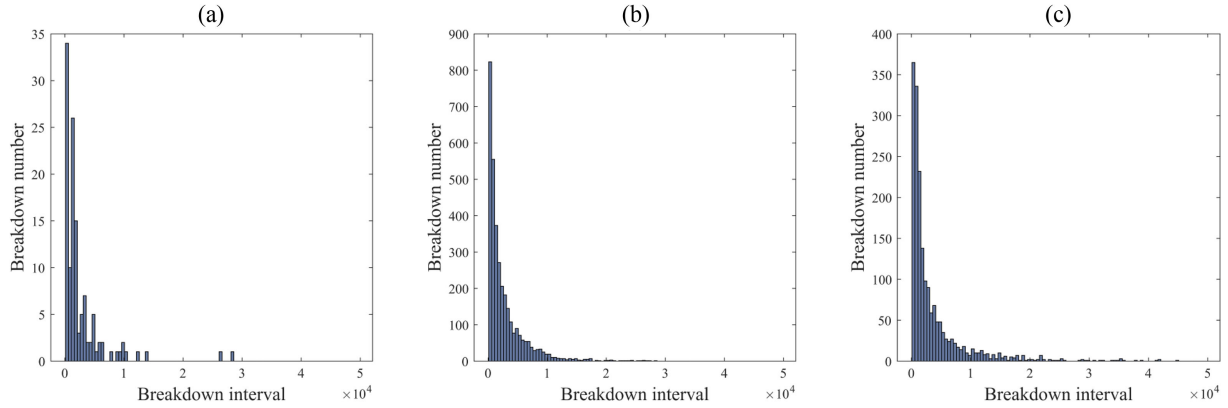


FIG. 10. rf breakdown interval distribution of XT72 No. 1, (a) for initial 200 breakdowns, (b) for breakdowns accumulated in first conditioning phase, and (c) for that of second phase.

width was changed from 80 to 120 ns. However, the breakdowns that occurred in the two phases of conditioning showed the same distribution trend. It indicates that the statistical distribution of breakdowns is independent of the pulse width. Figure 10 presents the distribution of the three stages of XT72 No. 1 as an example.

Prior research suggests that the evolution of the modified breakdown rate BDR* during conditioning follows a power-law relationship of the form [20]:

$$\mathrm{BDR}^* = C \times N^{\alpha}, \tag{8}$$

where C and α are fitting parameters, and N is the cumulative number of rf pulses. Figure 11 shows BDR* as a function of N for all six structures, with the corresponding power-law fits appearing linear on a log-log scale. The extracted parameters are listed in Table IV. Although XT72 No. 2 was conditioned with a full 120 ns pulse width from the start, its BDR* evolution trend was consistent with the other five structures—confirming the generality of the power-law relationship for X-band high-gradient structures. The power-law exponent α for the six XT72 structures ranges from -7.8 to -13.9, with a mean value of approximately -10. This average serves as a useful empirical benchmark for X-band structure conditioning, in agreement with results from TD26CC and TD24R05 structures [20]. While the overall power-law decay trend of BDR* is consistent across all structures, the significant variation in α highlights the sensitivity of the conditioning process. Notably, the conditioning evolution rates differed among the structures due to variations in rf waveform. As illustrated in Fig. 12, XT72 No. 4 and No. 5 were

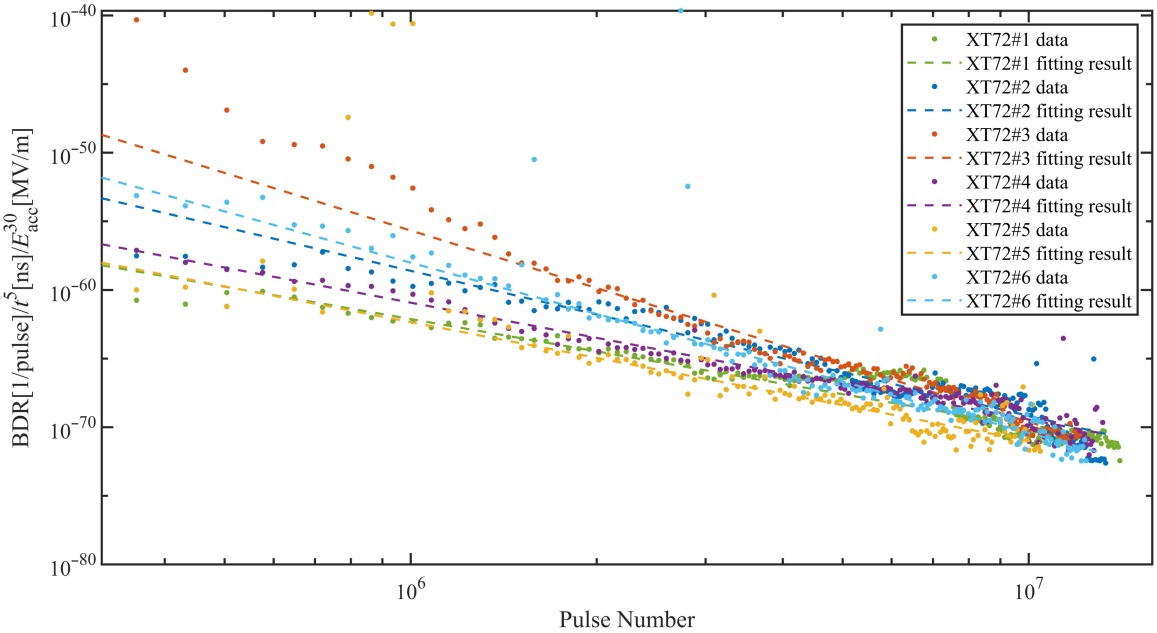


FIG. 11. Comparison of BDR* for six structures. The data are plotted in a log-log scale.

TABLE IV. Summary of power-law fit for the modified BDR.

Structure	α
XT72 No. 1	−7.8
XT72 No. 2	−10.6
XT72 No. 3	−13.9
XT72 No. 4	−8.5
XT72 No. 5	−8.6
XT72 No. 6	−12.4
TD26CC	−9.2
TD24R05 No. 1	−6.8
TD24R05 No. 2	−8.0

conditioned under impaired LLRF operation, resulting in input pulses with sharper rising edges and significant flattop droop. In contrast, the other structures received shaped pulses with slower edges and minimal droop. The former group exhibited slower BDR* reduction, which we attribute to the higher peak power—and correspondingly higher surface fields—required to maintain the same average gradient under drooping waveforms. This result highlights the importance of stable, flattop rf pulses for efficient and consistent high-gradient structure conditioning.

Despite identical rf design and manufacturing processes, the six XT72 structures exhibit notable variations in conditioning efficiency and BDR evolution, driven by a combination of structure-specific factors and procedural factors. XT72 No. 1 features the slowest conditioning rate ($\alpha = -7.8$) and highest cumulative breakdowns due to aggressive power stepping with short intervals, while XT72 No. 4 and No. 5 show delayed BDR reduction from impaired LLRF waveforms. This suggests that overly rapid power ramping can increase total breakdowns and slow asymptotic convergence to low BDR. The power-law exponent α varied from −7.8 to −13.9 across the set. Although an average near −10 provides a useful benchmark, the spread highlights the sensitivity of conditioning to structure-specific and procedural factors. Potential causes include minor differences in surface finish, local field enhancements from manufacturing tolerances, input waveform imperfections, and details of the power-stepping sequence. These observations collectively indicate that the conditioning process, while governed by a general statistical trend, remains influenced by individual structure properties and conditioning history, underscoring the critical importance of precise control over manufacturing quality, tuning fidelity, and rf waveform stability for reproducible and efficient conditioning of high-gradient accelerator structures.

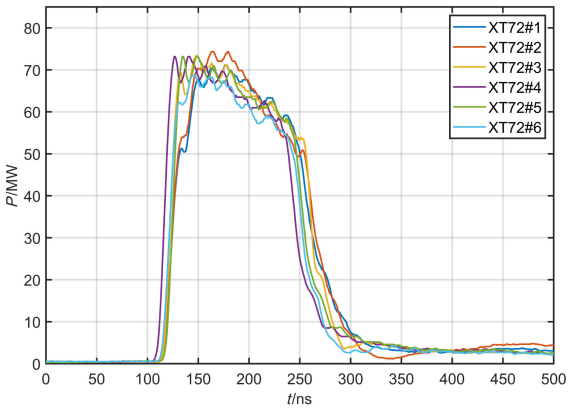


FIG. 12. Waveform of input power at 80 MV/m.

V. CONCLUSION

The X-band high-gradient accelerating structure is a critical enabling technology for the VIGAS project, meeting its stringent requirements for compactness and high performance. This paper has presented the comprehensive tuning, testing, and conditioning of six identical accelerating structures developed for VIGAS at Tsinghua University, all fabricated using the same rf design and manufacturing processes. Through meticulous low-power rf measurements, all six structures were successfully tuned, consistently achieving a reflection coefficient below −25 dB and an average phase advance of $120 \pm 0.1°$, thus fulfilling the design specifications. High-power conditioning demonstrated reliable operation at the target gradient of 80 MV/m with a breakdown rate below 1×10^{-4} per pulse. A detailed analysis of the conditioning data yielded several key insights. The spatial distribution of breakdowns was mapped, revealing a pronounced concentration in the front section of the structures. This localization showed a clear correlation ($R = 0.538$) with the simulated surface electric field, quantitatively validating that regions of higher surface field experience a greater breakdown probability. The evolution of the modified breakdown rate, BDR*, for all structures was found to follow a power-law decay, $\mathrm{BDR}^* = C \times N^{\alpha}$, with the exponent α clustering around −10, establishing a valuable empirical benchmark for X-band conditioning. Furthermore, statistical analysis of breakdown intervals using a two-exponential model confirmed that the underlying breakdown probability is largely independent of the rf pulse width, while also revealing structure-to-structure variations linked to differences in conditioning strategy and input waveform fidelity. The successful development and systematic characterization of these six structures not only validated the design and manufacturing approach for the VIGAS project but also provided significant practical insights for future X-band accelerator projects.

ACKNOWLEDGMENTS

This work was supported by the National Natural Science Foundation of China (NSFC Grant No. 12027902). We extend our sincere appreciation to the senior engineers at the Corporation Limited of Beijing

Huaqingjia High Energy Electron Technology for their invaluable assistance with fabricating and brazing work, including Jiaqi Qiu, Chuanjing Wang, Yunsheng Han, Jingzhong Xiao, and others. We also wish to express our gratitude to the students at Tsinghua Accelerator Laboratory, including An Li, Chongnan Shi, Hao Wang, Kede Jie, and Zhengkai Wang, who contributed to the high-power test experiment. Their contributions were invaluable, and we sincerely thank all participants for their dedication and support.

DATA AVAILABILITY

The data that support the findings of this article are not publicly available upon publication because it is not technically feasible and/or the cost of preparing, depositing, and hosting the data would be prohibitive within the terms of this research project. The data are available from the authors upon reasonable request.

[1] Y. Du, H. Chen *et al.*, A very compact inverse Compton scattering gamma-ray source, High Power Laser Part Beams **34**, 104010 (2022).

[2] L. Zheng, Y. Du, Z. Zhang *et al.*, Development of s-band photocathode rf guns at Tsinghua University, Nucl. Instrum. Methods Phys. Res., Sect. A **834**, 98 (2016).

[3] Q. Gao, H. Zha *et al.*, Design and test of an X-band constant gradient structure, Phys. Rev. Accel. Beams **27**, 090401 (2024).

[4] X.-C. Lin, H. Zha, J.-R. Shi, Q. Gao, J.-Y. Liu, L.-Y. Zhou, J. Gao, H.-B. Chen, and C.-X. Tang, Fabrication, tuning, and high-gradient testing of an X-band traveling-wave accelerating structure for VIGAS, Nucl. Sci. Tech. **33**, 102 (2022).

[5] X.-C. Lin, H. Zha, J.-R. Shi, L.-Y. Zhou, Y.-F. Liang, J. Gao, Q. Gao, H.-B. Chen, and C.-X. Tang, Design, fabrication, and testing of low-group-velocity s-band traveling-wave accelerating structure, Nucl. Sci. Tech. **33**, 147 (2022).

[6] H. Chen, L. Yan, Q. Tian, Z. Lin, D. Wang, C. Cheng, J. Shi, H. Zha, Y. Du, H. Chen, W. Huang, and C. Tang, Commissioning the photoinjector of a gamma-ray light source, Phys. Rev. Accel. Beams **22**, 053403 (2019).

[7] F. V. Hartemann, H. A. Baldis, A. K. Kerman, A. Le Foll, N. C. Luhmann, and B. Rupp, Three-dimensional theory of emittance in Compton scattering and x-ray protein crystallography, Phys. Rev. E **64**, 016501 (2001).

[8] R. Hajma, T. Hayakawa, N. Kikuzawa, and E. M. Minehara, Proposal of nondestructive radionuclide assay using a high-flux gamma-ray source and nuclear resonance fluorescence, J. Nucl. Sci. Technol. **45**, 441 (2008).

[9] D. Habs and U. Köster, Production of medical radioisotopes with high specific activity in photonuclear reactions with γ-beams of high intensity and large brilliance, Appl. Phys. B **103**, 501 (2011).

[10] K. Abe *et al.*, GLC project: Linear collider for TeV physics, Technical Report No. KEK-REPORT-2003-7, KEK, 2003.

[11] T. Higo, R. Zennaro, C. Adolphsen, L. L. Laurent, S. Döbert, A. Grudiev, G. Riddone, A. Jensen, J. W. Wang, S. G. Tantawi, S. Matsumoto, Y. Higashi, F. Wang, V. Dolgashev, W. Wuensch, and K. Yokoyama, Advances in X-band TW accelerator structures operating in the 100 MW/m regime, in *Proceedings of International Conference on Particle Accelerators* (2012), https://www.semanticscholar.org/paper/Advances-in-X-band-TW-Accelerator-Structures-in-the-Higo-Zennaro/ac7e55a0b79d5caacaf81edda157e976eda165de.

[12] A. Larsen, The next linear collider design: NLC 2001, Technical Report No. SLAC-R-571, Stanford Linear Accelerator Center, 2001.

[13] H. Hoag, H. Deruyter, C. Pearson, R. Ruth, J. Wang, and J. Schaefer, Accelerator structure development for NLC, in *Proceedings of International Conference on Particle Accelerators* (1993), Vol. 2, pp. 907–909, https://ieeexplore.iee.org/document/308734/.

[14] S. Döbert, Status and future prospects of CLIC, Technical Report, CERN, Geneva, 2009, https://cds.cern.ch/record/1155164.

[15] T. Higo, M. Akemoto, A. Enomoto, S. Fukuda, H. Hayano, N. Kudo, S. Matsumoto, T. Saeki, N. Terunuma, N. Toge, K. Watanabe, and T. Suehara, High gradient study at KEK on x-band accelerator structure for linear collider, in *Proceedings of the 21st Particle Accelerator Conference, Knoxville, TN, 2005* (IEEE Piscataway, NJ, 2005), pp. 1162–1164, https://ieeexplore.ieee.org/document/1590694

[16] A. Grudiev and W. Wuensch, Design of the CLIC main linac accelerating structure for CLIC conceptual design report, in *Proceedings of the 25th International Linear Accelerator Conference, LINAC2010*, edited by M. Ikegami, V. R. W. Schaa, and H. Sako (2011), MOP068, https://proceedings.jacow.org/LINAC2010/papers/mop068.pdf.

[17] S. Doebert, A. Grudiev, G. Riddone, M. Taborelli, W. Wuensch, R. Zennaro, S. Fukuda, Y. Higashi, T. Higo, S. Matsumoto, K. Ueno, K. Yokoyama, V. Dolgashev, L. Laurent, S. Tantawi, F. Wang, and J. Wang, High power test of a low group velocity x-band accelerator structure for CLIC, in *Proceedings of Linear International Accelerator Conference, LINAC08, Victoria, BC, Canada* (2008), https://proceedings.jacow.org/LINAC08/papers/thp061.pdf.

[18] W. Wuensch *et al.*, High-gradient test results from a CLIC prototype accelerating structure: TD26CC, in *Proceedings of the 5th International Particle Accelerator Conference (IPAC'14), Dresden, Germany* (JACoW, Geneva, Switzerland, 2014), pp. 2285–2287, 10.18429/JACoW-IPAC2014-WEPME015.

[19] T. Higo *et al.*, Comparison of high gradient performance in varying cavity geometries, in *Proceedings of the 4th International Particle Accelerator Conference, IPAC-2013, Shanghai, China* (JACoW, CERN, Geneva, Switzerland, 2013), WEPFI018, https://proceedings.jacow.org/IPAC2013/papers/wepfi018.pdf?n=IPAC2013/papers/wepfi018.pdf.

[20] A. Degiovanni, W. Wuensch, and J. Giner Navarro, Comparison of the conditioning of high gradient accelerating structures, Phys. Rev. Accel. Beams **19**, 032001 (2016).

[21] Q. Gao, Progress of accelerator system for the VIGAS project in Tsinghua University, https://indico.cern.ch/event/1080222/contributions/4844198/attachments/2445909/4190959/HG2022_Tsinghua_QG_upload.pdf (2022).

[22] A. Grudiev, S. Calatroni, and W. Wuensch, New local field quantity describing the high gradient limit of accelerating structures, Phys. Rev. ST Accel. Beams **12**, 102001 (2009).

[23] A. Grudiev, S. Calatroni, and W. Wuensch, Erratum: New local field quantity describing the high gradient limit of accelerating structures [Phys. Rev. ST Accel. Beams 12, 102001 (2009)], Phys. Rev. ST Accel. Beams **14**, 099902 (2011).

[24] D. P. Pritzkau and R. H. Siemann, Experimental study of rf pulsed heating on oxygen free electronic copper, Phys. Rev. ST Accel. Beams **5**, 112002 (2002).

[25] L. Laurent, S. Tantawi, V. Dolgashev, C. Nantista, Y. Higashi, M. Aicheler, S. Heikkinen, and W. Wuensch, Experimental study of rf pulsed heating, Phys. Rev. ST Accel. Beams **14**, 041001 (2011).

[26] C. W. Steele, A nonresonant perturbation theory, IEEE Trans. Microwave Theory Tech. **14**, 70 (1966).

[27] J. Shi, A. Grudiev, and W. Wuensch, Tuning of X-band traveling-wave accelerating structures, Nucl. Instrum. Methods Phys. Res., Sect. A **704**, 14 (2013).

[28] T. Khabiboulline, V. Puntus, R. Dohlus, N. Holtkamp, G. Kreps, S. Ivanov, and K. Jin, A new tuning method for traveling wave structures, in *Proceedings Particle Accelerator Conference* (1995), Vol. 3, pp. 1666–1668, 10.1109/PAC.1995.505321.

[29] M. Peng, D. Cao, W. Gai, Y. Jiang, J. Liu, J. Shi, and P. Wang, Development of Tsinghua X-band high power test facility, in *Proceedings of the 9th International Particle Accelerator Conference* (JACoW, Geneva, Switzerland, 2018), 10.18429/JACoW-IPAC2018-THPAL150.

[30] W. Wuensch, A. Degiovanni, S. Calatroni, A. Korsbäck, F. Djurabekova, R. Rajamäki, and J. Giner-Navarro, Statistics of vacuum breakdown in the high-gradient and low-rate regime, Phys. Rev. Accel. Beams **20**, 011007 (2017).

[31] A. Degiovanni, S. Döbert, W. Farabolini, I. Syratchev, W. Wuensch, J. Giner Navarro, J. Tagg, and B. Woolley, Diagnostics and analysis techniques for high power X-band accelerating structures, in *Proceedings of Linear Particle Accelerator Conference, LINAC 2014, Geneva, Switzerland* (JACoW, Geneva, Switzerland, 2014), https://proceedings.jacow.org/LINAC2014/papers/tupp029.pdf.

[32] Q. Chen, T. Hu, B. Qin, Y. Xiong, K. Fan, and Y. Pei, RF conditioning and breakdown analysis of a traveling wave linac with collinear load cells, Phys. Rev. Accel. Beams **21**, 042003 (2018).

[33] T. G. Lucas, J. Alex, C. Beard, A. Citterio, H.-H. Braun, P. Craievich, Z. Geng, R. Kalt, F. Loehl, M. Pedrozzi, J.-Y. Raguin, and R. Zennaro, Multiyear longitudinal analysis of vacuum breakdown and rf conditioning in the C-band linac of SwissFEL, IEEE Trans. Nucl. Sci. **72**, 781 (2025).

[34] L. Millar. Operation of multiple accelerating structures in an X-band high-gradient test StandResearch on backward traveling wave accelerating structures, Ph.D. thesis, Lancaster University, 2021, https://research.lancaster-university.uk/en/publications/operation-of-multiple-accelerating-structures-in-an-x-band-high-g/.

[35] W. L. Millar, A. Grudiev, W. Wuensch *et al.*, High-power test of two prototype x-band accelerating structures based on SwissFEL fabrication technology, IEEE Trans. Nucl. Sci. **70**, 1 (2023).